Composites Part B 252 (2023) 110510

Contents lists available at ScienceDirect

Composites Part B

journal homepage: www.elsevier.com/locate/composites

Intralaminar crack growth rates of a glass fibre multiaxial laminate subjected to variable amplitude loading

J.J. Bender [a,*], B.L.V. Bak [a], L. Carreras [b], E. Lindgaard [a]

[a] CraCS Research Group, Department of Materials and Production, Aalborg University, Fibigerstraede 16, DK-9220, Aalborg East, Denmark[1]
[b] University of Girona, AMADE, Polytechnic School, C/Universitat de Girona 4, 17003 Girona, Spain

ARTICLE INFO

Keywords:
Variable amplitude
VCCT
Intralaminar cracking
Crack density
Finite element method

ABSTRACT

The literature shows that variable amplitude loading can be much more severe than constant amplitude loading in a fatigue damage context. However, the underlying physical explanations for this are still unknown. Therefore, this paper investigates if the local energy release rate at each intralaminar crack tip in a tension/tension fatigue loaded multidirectional laminate can be used to determine the crack growth rate of these cracks subjected to variable amplitude loading. The local energy release rate is investigated through a developed finite element model in which any number of cracks can be included to account for their interaction. The position of the cracks is determined based on previous experimental work. The experimental results from the previous work are compared to the numerical results in this work. At similar crack density levels the energy release rates increase in the variable amplitude tests compared to constant amplitude tests, but not enough to significantly impact the crack growth rate. It is concluded that less than 5% of the increased crack density rate and crack growth rate caused by variable amplitude block loading is due to increases in local energy release rate. The primary reason is more likely found on a microstructural level.

1. Introduction

Fatigue failure of composite structures is a complex problem conditioned by a long list of parameters [1–3]. One of which is the load conditions. The loads in actual structures that cause these fatigue failures are variable in terms of, e.g. magnitude and frequency. There are some repeating patterns in the load, but the load history of, e.g. a wind turbine blade, is far from a constant amplitude (CA) cyclic loading condition [4] from which material properties are derived [5]. It has been shown in recent studies [6–8] by the authors that the load history can have a significant effect on the damage evolution rate. This means that the fatigue life can be overpredicted if it is based on CA material characterisation. The damage evolution rate is typically defined as the delamination growth rate for interlaminar damage or the matrix crack density rate for intralaminar damage.

The prevailing theory in the literature for the load history effect is a so-called cycle mix effect [9–13]. The general understanding of this effect is that additional damage occurs every time the load condition changes. Additional damage could be delamination or matrix crack growth, and the load condition refers to mean load, load amplitude, or maximum load. The cycle mix effect has been detected for interlaminar [7,8] and intralaminar [6,9–13] damages. The underlying mechanisms behind this development in damage have not yet been identified. This work focuses on the intralaminar damage developing under variable amplitude loading for multidirectional laminates.

In [13], it is shown experimentally that a random load spectrum is much more damaging than high to low and low to high sequences when assessed by residual strength. The authors state that the reason for this is unknown. It was recently possible in [14] to simulate the experimental results from [13]. In [14], a residual strength model is used, which considers the strength reduction of all loading blocks in the order they are applied. The model does not include any cycle mix factors to arrive at the result. This also means that the model cannot account for any non-linear transition effects [6–8], as these effects would not be present in the residual strength master curves.

A potential cause for the cycle mix effect could be changes on the micro scale due to load history. In the literature, it has been considered multiple times that one of the reasons for fatigue damage in scenarios with shear loads is diffuse damage [15–18]. Diffuse damage is defined as matrix/fibre debonds and microcracks in the matrix. It has also been shown that diffuse damage influences the damage evolution in static load scenarios [19,20].

* Corresponding author.
E-mail addresses: bender@mp.aau.dk (J.J. Bender), brianbak@mp.aau.dk (B.L.V. Bak), lcb@mp.aau.dk (L. Carreras), elo@mp.aau.dk (E. Lindgaard).
[1] cracs.aau.dk

https://doi.org/10.1016/j.compositesb.2023.110510
Received 4 September 2022; Received in revised form 18 December 2022; Accepted 4 January 2023
Available online 7 January 2023

In [15,16], diffuse damage is used as the only parameter to decrease the fracture toughness of the material in order to develop fatigue damage growth. In [17], it is experimentally shown that increased diffuse damage on the micro scale increases the macro crack density at similar static load levels. Carbon Fibre Reinforced Polymer (CFRP) specimens are loaded statically in shear at different load levels to induce diffuse damage. Subsequently, the tested specimens are cut into smaller specimens and tested in static tension. The higher the shear strain, the higher the crack density in static tension. In [18], it is shown that diffuse damage in the form of shear cusps can occur in front of the crack tip in Glass Fibre Reinforced Polymer (GFRP) specimens for a fatigue shear load case. For the static case in [19], an Arcan fixture is used to cause pure shear load in CFRP cross-ply specimens to induce diffuse damage. The specimens are then rotated to cause pure normal loading. It is reported that the diffuse damage caused a decrease in normal strength of up to 17.5% compared to a specimen with no diffuse damage. In [20], it is shown that by including diffuse damage in the simulation models, the experimental results of the static tension test in a CFRP cross-ply laminate are more accurately represented.

Common for the cited works here is that diffuse damage has been induced in a shear load case. In [21], CFRP cross-ply specimens are loaded in cyclic normal tension fatigue. It is shown that the diffuse damage caused by the fatigue loading has little to no effect on the static evolution of intralaminar damages in a pure mode I load case. This shows that diffuse damage most likely only occurs in scenarios with shear load.

Whether this diffuse damage should be included in prediction models is still undecided, as is the case for the cycle mix effect. Some researchers have included the cycle mix effect in phenomenological prediction models without proposing an origin of the effect [14,22–25]. In [26], a progressive fatigue prediction model is developed to account for VA loading [26]. In [26], the load sequence effect is included through a strain evolution curve, and, as a result, the diffuse damage is not explicitly accounted for.

On the other hand, in the previous experimental work [6] by the authors. It is shown that the cycle-mix effect affects the crack density growth rates significantly. It is hypothesised that the inherent inhomogeneities of the material could cause cracks in CA low loading (CA-L) to slow down in tough material points, which would decrease the crack density rate. In contrast, in the VA load case, crack growth rates could also decrease in tough material points during a VA low load block (VA-L), but a block of high loads would allow the crack to propagate through the tough material points and continue at a high propagation rate. Furthermore, there is a clear difference in the distribution of the number and length of cracks at similar crack density levels, specifically between CA-L loading on one side and CA High (CA-H) loading and Variable Amplitude (VA) loading on the other. This can be a potential reason for the cycle-mix effect, i.e., the stress distribution is affected by the configuration of cracks, meaning location, lengths, and quantity of cracks.

In the literature, it has been shown that the stress field around a crack is affected by neighbouring cracks and that the stress intensity factor and, hereby, the Energy Release Rate (ERR) can increase and decrease significantly [27–29]. For a 2D case, the ERR can increase by a factor of two compared to just a single crack depending on the crack size and relative locations [27,29]. For a 3D case, the effect is smaller but still present [28]. This shows that the configuration of cracks can increase the local ERR at a crack tip compared to an isolated crack.

This brief review shows that the physical explanations behind increased damage progression in VA loading cases are still unknown. Diffuse damage can be essential in damage progression in shear load cases in static and fatigue. However, diffuse damage has not been incorporated in the modelling and prediction of fatigue failure of VA loading cases, and the effect of diffuse damage has not been investigated concerning VA loading either. Finally, cracks in close vicinity can experience increased and decreased ERR compared to a situation with isolated cracks.

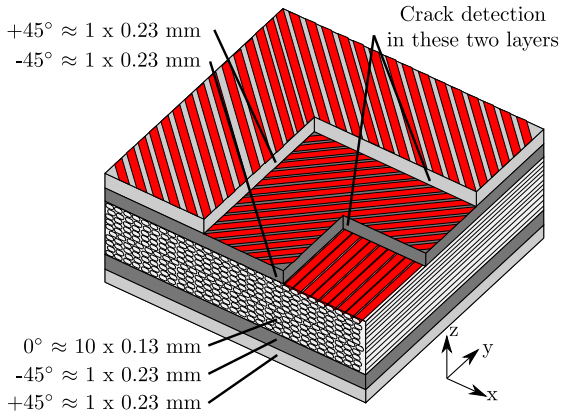

Fig. 1. Illustration of the lay-up of the manufactured specimens.

1.1. Research questions

The introduction leads to the following research hypothesis:

The increased crack density rate in VA loading cases can either be caused by local increases in ERR, local decreases in fracture toughness due to diffuse damage, local variations in material toughness, or a combination of the three.

A higher ERR is related to a higher Crack Growth Rate (CGR) if the cracks in the multidirectional laminate follow a Paris law-like relation [2]. Therefore, by investigating the ERR and CGR of the crack tips in the CA and VA tests, it can be determined if the distribution of cracks affects the ERR to the extent as to cause changes in the CGR. The hypothesis is investigated through the following research questions:

1. How are the ERR and CGR at each crack tip affected by the local load conditions?
2. Can a Paris law-like relation be used to determine the effect of variations in ERR from CA to VA?

The remainder of this paper is organised as follows. Section 2 describes the parametric FE model used to investigate the interaction of matrix cracks. Section 3 presents the experimental results from [6] and the current numerical results regarding the ERR of the individual crack tips. Section 4 discusses the results and how a Paris law-like relation can be used to quantify the effect of variation in ERR. Finally, Section 5 presents the final concluding remarks.

2. Parametric FE model

A parametric FE model has been developed that includes all discrete cracks as they appear in experimentally tested specimens. This way, it is possible to simulate the complex and interacting stress fields of multiple cracks and determine the ERR at every crack tip in the tested specimens as the test progresses. A description of the experimental campaign and the results can be found in [6] by the authors. The specimens were made from epoxy and glass fibres, with a lay-up as shown in Fig. 1. The specimens were loaded parallel to the fibres in the centre of the laminate.

The tests were performed in uniaxial tension–tension fatigue. Images based on transillumination were acquired throughout the tests to monitor the initiation and propagation of all the matrix cracks in the two layers closest to the camera. A zoom-in on one of the resulting raw images is shown in Fig. 2. This type of high-resolution image-based crack tracking algorithms are becoming more widespread [6,8,30–35], indicating the usefulness of such methods.

The concepts of the parametric model are described in this section. As shown in Fig. 1, there are 14 layers. Due to the symmetry of the laminate, only half the thickness is modelled. There are ten steps in

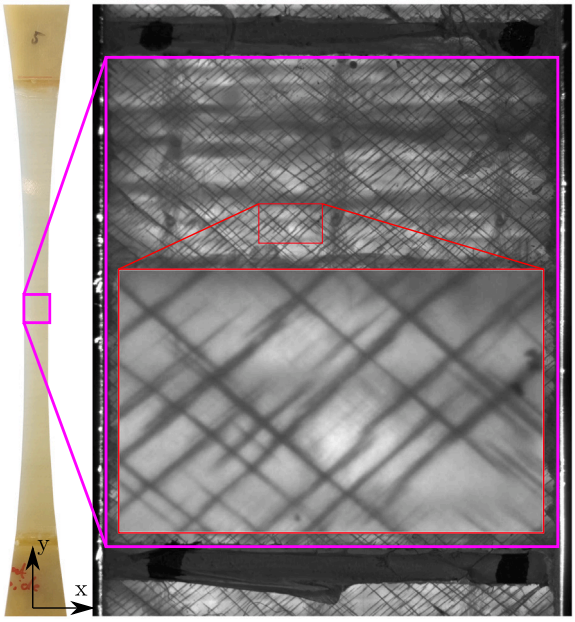

Fig. 2. One of the used test specimens is shown to the left, where the measuring area of a specimen is indicated with the magenta box and a zoom in of raw cracks from fatigue testing is indicated by the red box. (For interpretation of the references to colour in this figure legend, the reader is referred to the web version of this article.)

building the FE model, which are described below and illustrated in Fig. 3:

1. For each layer, create areas according to the boundaries of the measuring area.
2. Create areas around all crack locations in both cracking layers.
3. Create structured mesh in crack areas.
4. Create a free mesh to connect the crack areas in each layer.
5. Extrude the 2D area mesh in the thickness direction of the layer.
6. Rotate the elastic material properties according to the crack areas.
7. Create mesh discontinuities at crack surfaces to create discrete cracks.
8. Tie layers together with Multi-Point Constraints (MPC).
9. Apply boundary conditions.
10. Calculate ERR based on VCCT at each crack tip.

The points above are detailed further in this section.

2.1. Create boundary and crack areas

The modelled area corresponds to approximately 80% of the measuring area in the experiments. With the required mesh size, it was not practically possible to simulate the entire measuring area due to memory restrictions on the hardware (500 GB of RAM). The 80% was selected, so the entire width in the x-direction was included, and 80% of the measuring height in the y-direction, starting at y = max(y). The location of all crack tips was known from the crack counting algorithm [6,30]. These locations were used to generate an area around each crack, with a buffer in the crack growth direction. This buffer was used to ensure a structured mesh in front of the crack tip, which is necessary to calculate the ERR accurately based on VCCT. In the current model, up to 1000 cracks have been included in each layer.

2.2. Create structured and free mesh

All the meshed crack areas were connected with a free mesh of primarily quadrilateral elements with an element side length of 0.075 mm. The elements in the crack areas were 0.05 mm in the length direction of the crack and 0.01 mm perpendicular to this. The smaller dimension perpendicular to the crack length was to allow cracks to be closer to each other without crack areas overlapping.

2.3. Overlapping crack areas

Some crack areas overlap even with the small dimension perpendicular to the crack direction. For the simulated specimens, this is less than 5% of cracks, and therefore the smallest of the overlapping cracks is not included in the simulation. There was no significant difference in the number, length, or location of the deleted cracks between the load cases. This renders the stress field around the missing cracks inaccurate. Therefore it has been decided that any crack tips within a radius of four times the layer thickness to an excluded crack are not included in the post-processing. This is illustrated in Fig. 4. The red crack in the centre illustrates an excluded crack, and the red circles indicate the exclusion radius. Five crack tips are excluded within the circles, indicated by the red crosses. Furthermore, any crack tips closer than four times the layer thickness to the upper and lower boundary, blue boxes in Fig. 4, are not considered since any crack tips on the outside of these boundaries are not included in the simulation. Therefore stress fields in these regions are also inaccurate. Finally, all crack tips closer than four times the layer thickness to the edges of the specimen, red boxes in Fig. 4, are omitted. In the simulation, the crack tips close to the edges are all embedded in the specimen, meaning that the crack tips have not reached the edges, even though this is most likely the case in the experiments. This is done to ease the automatic meshing. However, it also entails a discrepancy between the simulation and experiments at the edges, which is why the crack tips at the edges are omitted from post-processing.

2.4. Extrude 2D mesh in the thickness direction

The created 2D mesh was extruded in the thickness direction of the plies. For the 45° / −45° layers, there are two elements in the thickness direction to allow the layer to open at the cracks. A model at smaller scale has been used to verify that the solution is indeed converged. For six quadratic elements through the thickness the difference in ERR is less than 2%. The constraining 0° layer has only one element in the thickness direction. After the extrusion, the total number of elements is approximately $2.6 \cdot 10^6$ elements, where $1.5 \cdot 10^6$ are solid elements, and the rest are contact elements for the MPCs. The solid elements used in this work are ANSYS SOLID186 20-node brick elements exhibiting quadratic displacement behaviour.

2.5. Rotating material coordinate systems

The element and material coordinate systems have been rotated in the 45° / −45° layers to be aligned with the fibre direction. However, it is apparent from the images obtained in the experiments that not all cracks are aligned in the same direction, and therefore neither are the fibres. Therefore, to align the principal material direction with the fibre orientation, the element coordinate systems have been aligned with the crack direction of each crack area to avoid having a bi-material interface at the cracks. The elements in the free mesh between the crack areas have been aligned with the mean angle of the crack areas.

2.6. Create discrete cracks

The crack surfaces have been created by removing the connectivity of the elements on either side of the crack surface by introducing more nodes. However, the elements on either side of the crack face share nodes in the interface to other plies since the actual cracks will not be open in these interfaces either. Some opening will occur in the interfaces when local delaminations start, but for the considered damage state, only a negligible amount of local delaminations have been initiated.

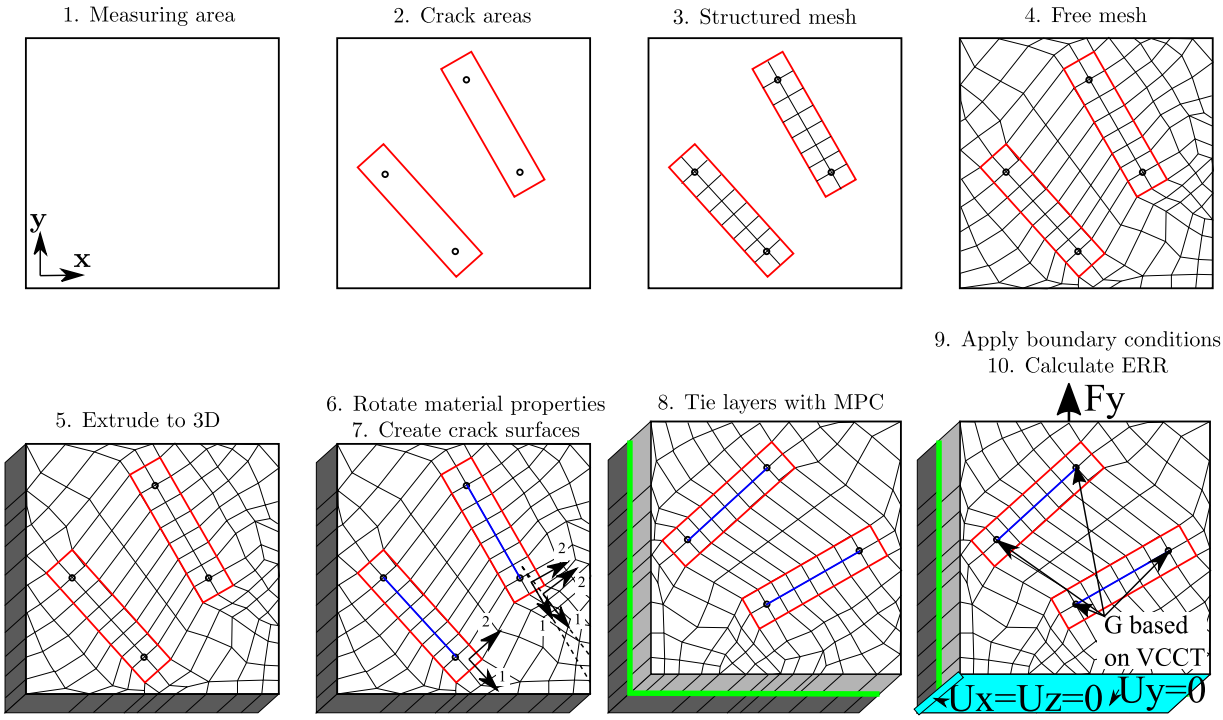

Fig. 3. Building the FE model. (For interpretation of the references to colour in this figure legend, the reader is referred to the web version of this article.)

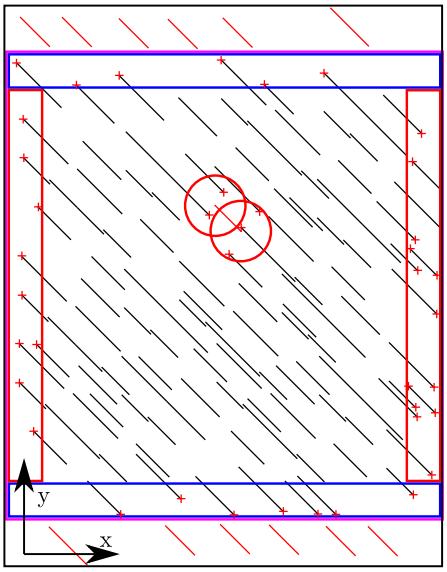

Fig. 4. Illustration of the crack exclusion criteria. The crack tips with red crosses have been excluded. (For interpretation of the references to colour in this figure legend, the reader is referred to the web version of this article.)

2.7. Tying layers together with MPC

The above steps have been followed for the +45 and −45 degree layers, and then they are tied together with MPCs since the meshes are different. The MPCs (green lines in Fig. 3_8) are used to tie the constraining layer and the cracking layers together. This method was chosen to have a coarser mesh in the constraining layer to reduce computational time and relatively simple meshes in the cracking layers. This means that the layers can be modelled independently. The always bonded contacts are enforced using the internal MPC algorithm in ANSYS, which reduces the total degrees of freedom in the model. A small-scale study has been conducted to investigate the error caused by using MPCs compared to compatible meshes. For a simple case with two adjacent layers and one crack in each layer, there was a difference in calculated ERR of around 5%. The overall trend concerning which crack configurations caused increased and decreased ERR was the same, but the absolute values were off by 5% on average.

2.8. Applying boundary conditions

The boundary conditions have been imposed on the nodes, as shown in Fig. 5. Displacement constraints have been applied in the y-direction at y = 0, and at x = y = 0, the nodes have been constrained in the x-direction. Symmetry conditions have been applied on all nodes at z = 0. At y = max(y), a load is applied to a single master node, and all other nodes on the surface are constrained to the same displacement in the y-direction.

2.9. Calculating ERR based on VCCT

Finally, the ERR is calculated at each crack tip after the simulation has been completed. The simulations in this work are solved as linear static analyses. The ERR is calculated based on the Virtual Crack Closure Technique (VCCT) described in [36]. Recent developments of advanced cohesive zone models for progressive damage simulation are more computationally efficient than previously [37–39]. However, they are still not as fast as VCCT if the only result needed is the ERR, as in this work. VCCT is used in this work as a compromise between computational efficiency and accuracy. 0 An accurate representation of the stress field around the crack tip is required for the VCCT to be accurate. This requires a fine mesh, but the mesh also has to be fine to model the crack tips that are close to each other as well. Therefore, this requirement for the VCCT does not require an extra computational effort. Direct application of the J-integral approach initially introduced by [40] is not applicable due to closely spaced interacting crack tips and is further complicated by orthotropic properties. As an alternative to the VCCT method applied, the recently developed J-integral for cohesive interfaces in 3D structures [41–43] could be applied. However, this

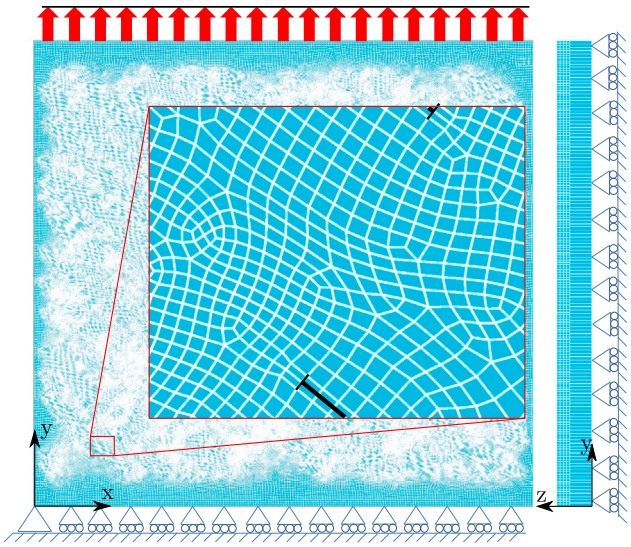

Fig. 5. Illustration of the imposed boundary conditions and the generated mesh on the top surface, and a zoom in on a region with two cracks with one visible crack tip each (indicated with black lines).

would require that every crack is described and discretised by cohesive elements, leading to high numerical costs.

With a working FE model, it is possible to couple the calculated ERR at every crack tip in the specimen with the corresponding experimentally obtained CGR.

3. Results

3.1. Brief summary of experimental results in [6]

The results presented in this paper are derived based on the experiments conducted in previous work by the authors [6]. A summary of the results from the previous work by the authors is presented here to aid the reader in understanding the results in the current work.

An experimental campaign with 11 specimens was conducted, three specimens at a CA-H and CA-L maximum cyclic load, respectively, and five specimens with two-block VA cyclic loading.

One of the primary results was that the crack density rate, i.e. how much the crack density increased over a given number of cycles, was affected by the load history. The crack density, ρ, in [6] and the current work is defined as

$$\rho = \frac{\Sigma_{i=1}^{n} L_i}{A_{\mathrm{m}}} \tag{1}$$

where L_i is the length of the i'th crack, and A_{m} is the measuring area. An example of the increased crack density rate is shown in Figs. 6 and 7.

In Fig. 7, it is shown that the crack density rate is significantly higher in the Variable Amplitude Low load blocks (VA-L) than in the CA-L at similar crack density levels. The VA-L curves are generated based on the average crack density rate in the transition and constant rate phase in each VA-L block. This results in a series of ≈ 10 discrete points for each specimen in the plot, which are connected with lines. For the curves with min/max bands multiple specimens are used to determine the mean curve. Therefore, the mean curve can have up to ≈ 20 discrete points, since the crack density level for each VA-L block is not necessarily the same for each specimen. In this work and [6], the crack density level is considered identical to the damage state. The transition and constant rate phase in Fig. 7 are illustrated in Fig. 6. All VA-L blocks are divided into these two phases based on a MATLAB function 'findchangepts'. This MATLAB function can fit multiple straight lines to a dataset while minimising the residual error. What has not been determined from the previous experimental work but studied in the current work is how the load history affects the individual crack tips.

3.2. Description of data extraction

The current work explores the load history effect by examining the ERR and CGR at the crack tips for CA and VA, respectively.

The results are based on the crack data from layer 1 (Surface layer) because the cracks in this layer generally propagate more. The CGRs are determined based on the change in location of each crack tip at the beginning and end of each interval, i.e. from the beginning of a VA-H block to the end of the same VA-H block. The same goes for the VA-L transition phase and constant rate phase. The ERR is determined through an FEA in the middle of the interval, as indicated in Fig. 6 by the red crosses. Furthermore, the red crosses indicate that FEAs are conducted at similar crack density levels for the CA-H and CA-L, as indicated in Fig. 6. The data from the different FEA are kept separate in this section to compare CA and VA data at similar crack density levels.

3.3. ERR and CGR at same crack density level

Figs. 8–10 show two histograms each. The top one shows the distribution of ERR of all considered crack tips. The bottom histogram shows the distribution of CGR of the same crack tips. The data in each dataset is arranged into ten bins where the mean value of the bin is located at the markers on the curves. The width of the bins is equal to half the distance to the neighbouring markers. The data in the histograms have been extracted from the FE model, and the experimental data at the same crack density levels around 1.2 mm^{-1} for CA-H, CA-L, and VA specimens. It is observed experimentally that the CGR of cracks in VA-H is higher than at the corresponding crack density in CA-H, as shown in Fig. 8b. This is indicated by the shift to the right of the VA-H data (green curve) compared to the CA-H data (red curve). Furthermore, the distribution of cracks causes a slight shift in the ERR, as shown in Fig. 8a, where the peak is shifted from 120 to 170 $\mathrm{J/m}^2$.

For the VA-L transition phase and CA-L, there is an apparent increase in CGR in the VA-L transition phase of multiple decades, as shown in Fig. 9b. However, unlike in the VA-H case, it does not seem that there is any systematic increase in ERR, as shown in Fig. 9a.

Finally, for the CA-L and VA-L constant rate phase, there is an increase in CGR (Fig. 10b) but less than in the transition phase. Some of the ERR distribution peak seems to be shifted from 30 $\mathrm{J/m}^2$ to 55 $\mathrm{J/m}^2$ in the VA-L constant rate phase compared to the CA-L, as shown in Fig. 10a. Indeed, the tendency of a shifted peak of the ERR distribution is comparable in Figs. 10a and 8a.

3.4. Paris law-like relation

The relation between ERR and CGR is considered in this work. This enables to link the experimentally determined changes in CGR to the simulated ERRs. All crack tips in the specimens are affected by load history effects, even in the CA load cases. The load at each crack tip changes throughout the tests due to load distributions from other propagating cracks [44]. Therefore, it is expected that a Paris law-like relation cannot produce a perfect relation between the ERR and CGR, but it is used to quantify the effect of the changed ERR due to VA loading in the lack of a better method. As confirmed in Fig. 11, the individual crack tips in the specimens do not exhibit any significant Paris law-like relation based on the shallow slope of the Paris law-like fit for the CA-L, CA-H, VA-L, and VA-H data, respectively. This indicates that the variation in ERR due to stress redistributions causes

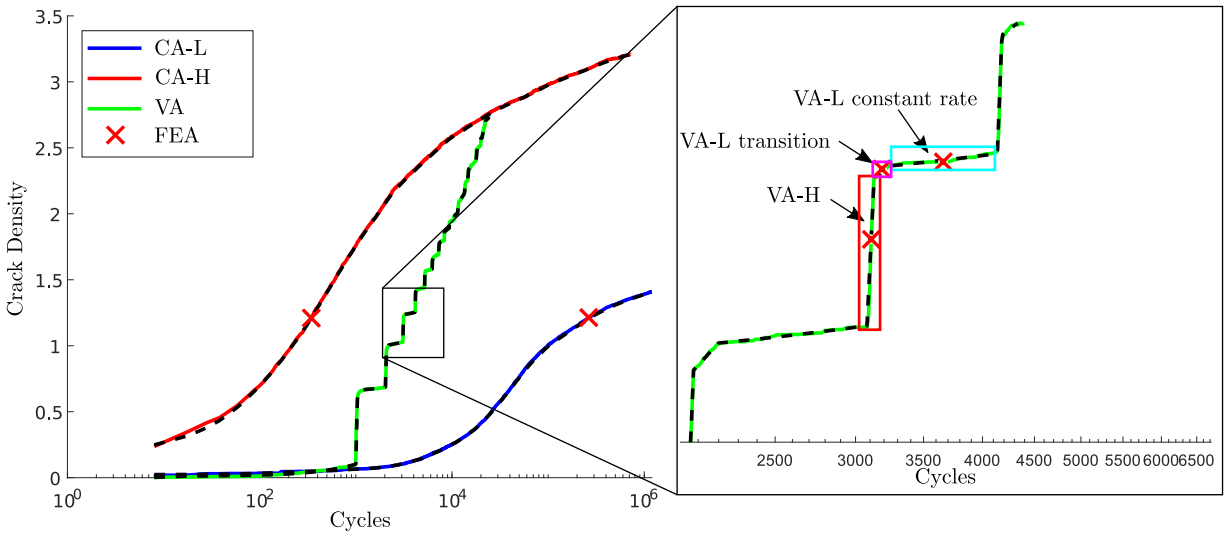

Fig. 6. Example of crack density as a function of cycles for CA-L, CA-H, and VA tests from [6]. (For interpretation of the references to colour in this figure legend, the reader is referred to the web version of this article.)

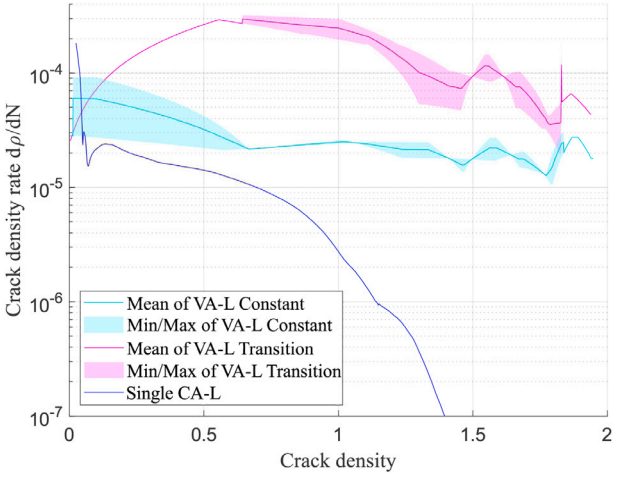

Fig. 7. The crack density rate as a function of the crack density for CA-L and VA-L. (For interpretation of the references to colour in this figure legend, the reader is referred to the web version of this article.)

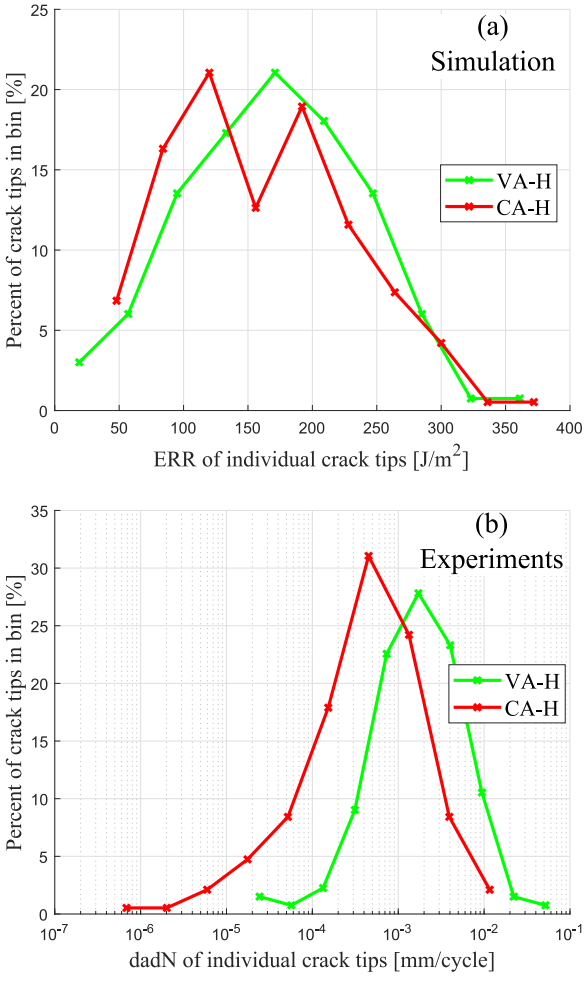

Fig. 8. Histogram of the distribution of (a) ERR based on simulations, and (b) CGR based on experiments for all the crack tips in CA-H and VA-H at $\rho = 1.14$ mm^{-1}. (For interpretation of the references to colour in this figure legend, the reader is referred to the web version of this article.)

no systematic change in CGR. Furthermore, it does not seem to be the case that a single Paris law like curve can fit all the data.

However, considering all the data points from a CA-L and CA-H test at around 1.2 mm^{-1} crack density, it is possible to estimate a Paris law-like relation. The mean of the CA-L and CA-H data are used as two points in the regression, as shown in Fig. 12.

4. Discussion

This discussion will focus on the research questions presented in Section 1 based on the results in Section 3. The first research question concerns how the load conditions affect the ERR and CGR. Figs. 8a and 10a show that more crack tips with higher ERR exist in the VA load cases compared to the CA load cases. This indicates that the distribution of the cracks affects the ERR of the individual cracks in an average sense. However, it is uncertain if the increased ERR is enough to account for the increased CGR, as shown in Figs. 8b and 10b. Therefore, an attempt to quantify the effect of the increased ERR is presented here to answer the second research question regarding how a Paris law-like relation can be used to determine the effect of variations in ERR between CA and VA load cases.

The overall idea is to quantify the effect of the increased ERR in the VA load case by assuming a Paris law-like relation between the CA-L

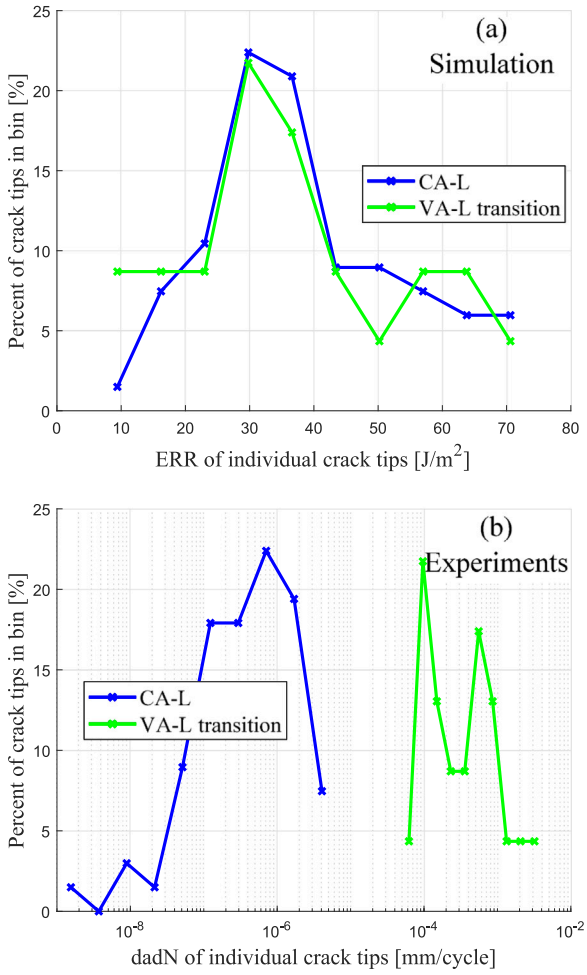

Fig. 9. Histogram of the distribution of (a) ERR based on simulations, and (b) CGR based on experiments for all the crack tips in CA-L and VA-L transition phase at $\rho = 1.23$ mm^{-1}. (For interpretation of the references to colour in this figure legend, the reader is referred to the web version of this article.)

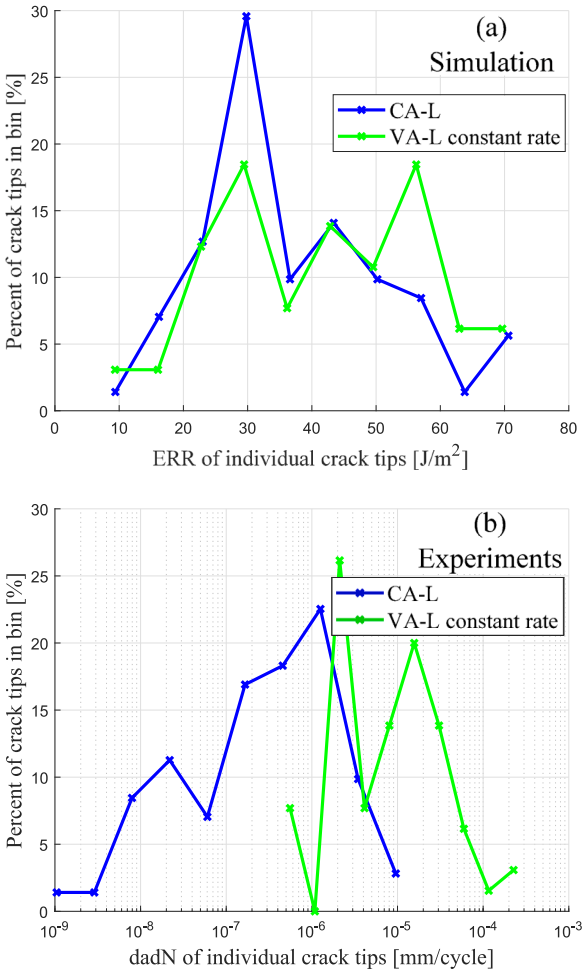

Fig. 10. Histogram of the distribution of (a) ERR based on simulations, and (b) CGR based on experiments for all the crack tips in CA-L and VA-L constant phase at $\rho = 1.24$ mm^{-1}. (For interpretation of the references to colour in this figure legend, the reader is referred to the web version of this article.)

and CA-H load cases, as shown in Fig. 12. This relation can then be used to calculate the CGR of the crack tips in CA and VA and compare these calculated CGRs with the experimentally obtained CGRs. The CGR of all crack tips has been calculated by combining the Paris law-like relation in Eq. (2) [45] with the ERR of all the crack tips in the individual simulations. E.g., the ERR data from the red and green curve in Fig. 8a is used as input, G, in Eq. (2) to determine a calculated CGR, which is then plotted in Fig. 13c.

$$\frac{da}{dN} = C \cdot G^m \tag{2}$$

Where C is the coefficient and m is the exponent of the Paris law-like curve, respectively. Based on the data in Fig. 12 and regression $C = 1.006\ \mathrm{e}^{-14}$ and $m = 4.997$. Based on the Paris law-like expression, it is possible to quantify the effect of the shifted histograms of the ERR and determine how it affects the distribution of CGRs.

Figs. 13a–b show the same data as in Figs. 8b and 10b, respectively, for easy comparison to Figs. 13c–d, respectively. Fig. 13c–d show the resulting CGR from Eq. (2) based on the ERR shown in Fig. 8a and 10a. The histogram curves for the high load case (Figs. 13a and c) show a comparable distribution for the CA-H load (red). The minimum and maximum bins are more extreme in the calculated histogram (Fig. 13c), but the overall shape of the distribution is comparable. The peak in Fig. 13a has been smoothed out to the neighbouring bins, possibly

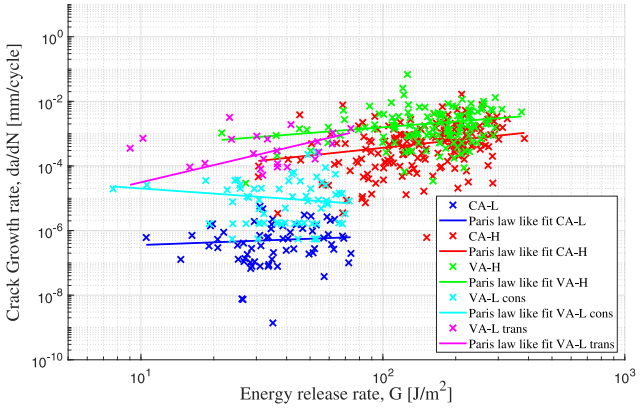

Fig. 11. ERR from a single FEA, and CGR from image processing for CA-H, red crosses, CA-L, blue crosses, VA-H, green crosses, VA-L constant rate phase, cyan, and VA-L transition phase, magenta, respectively. The coloured lines indicate the Paris law-like relation of the crack tips in the respective data sets. (For interpretation of the references to colour in this figure legend, the reader is referred to the web version of this article.)

due to the variability of the underlying data. For the CA-L constant case, as shown in Figs. 13b and d, there is a comparable shape of the distribution of the blue curves, and the minimum and maximum values

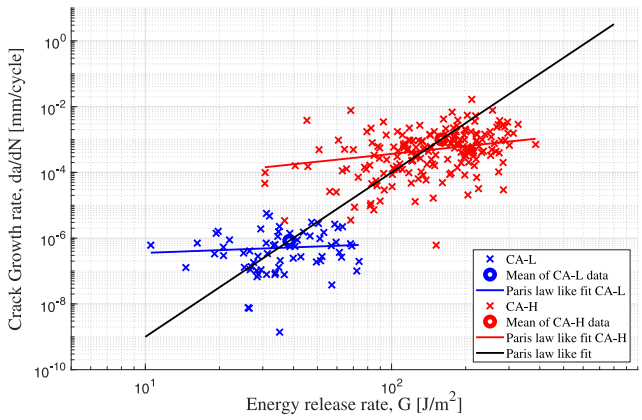

Fig. 12. ERR from a single FEA, and CGR from image processing for CA-H, red crosses, and CA-L, blue crosses, respectively. The black line represents the linear regression between the two swarms of data points, i.e. through the mean of each swarm. The blue and red lines indicate the Paris law-like relation of the crack tips in the CA-H and CA-L load cases, respectively. (For interpretation of the references to colour in this figure legend, the reader is referred to the web version of this article.)

seem to be reasonably close. The fact that the CA data is represented fairly accurately through this Paris law-like relation means that it can be used to estimate the effect of the changes in ERR in the VA load case compared to the CA load cases.

For the high load case in Fig. 13a, there is a clear difference in the distributions' peak and the mean of the distributions (indicated by the dashed vertical lines). The difference in mean CGR is by a factor of 3.3. When considering Fig. 13c, the shape of the VA-H distribution is changed to be more similar to the CA-H distribution. The slight shift of the ERR distribution shown in Fig. 8a results in a similar shift in the CGR in Fig. 13c, and the mean value is now only 1.09 times higher in VA-H.

The change in ERR would have had no effect on the CGR if the mean values were the same in Fig. 13c, and the ERR would have been the sole reason for the increased CGR if there had been a factor of 3.3 between the mean values of the CA-H and VA-H in Fig. 13c. However, with the factor of 1.09, this corresponds to ≈ 4%, i.e., the change in ERR from CA to VA is responsible for 4% of the increased CGR based on this calculation. It should be noted that by using the mean in log scale compared to the linear scale, used in this work, this value changes to 13%. Therefore, the actual value should be considered as an estimate.

For the VA-L constant rate phase in Figs. 13b and d, it is clear that the VA-L experimental data (Fig. 13b) changes shape quite significantly, and the mean value is decreased by almost a decade for the calculated data (Fig. 13d). Furthermore, the mean value of the CA-L data is increased from the experiments to the calculated histograms. The result is that the mean values are moved much closer to each other, and hereby using the same logic as before, the change in ERR from CA to VA is responsible for 2% of the increased CGR.

Due to the large scatter of data in Fig. 12, it is questionable whether the Paris law-like relation is appropriate in this case. However, it is chosen as the best option nonetheless. The fact that only 2%–4% of the increased CGR in VA compared to CA is caused by changes in ERR indicates that the configuration of cracks has minimal effect on the CGR of the individual cracks in the specimen in an average sense. Therefore, other effects are causing the increase in CGR, presumably microstructural effects that are not included in the modelling framework. There are at least two different microstructural effects that could influence these results. The first is the hypothesis by the authors [6] that tough material points reduce the CGR in CA-L. This would yield higher CGR in VA-L compared to CA-L, however, this has not been investigated extensively in the current work. Instead one could consider the data in Fig. 12. The region with high ERR and low CGR (lower right corner of each data set) should be more heavily populated with data in the CA-L compared to VA-L. This does not seem to be the case, therefore, it may not be concluded that tough material points are the only contributor to the difference in CGR. This hypothesis can, however, not explain the increased CGR in VA-H compared to CA-H, but the diffuse damage can. The diffuse damage will develop during the low load blocks as microdamage in the material and also in front of the crack tips. This microdamage may coalesce at the next high load block, increasing the CGR.

5. Conclusion

This work investigates the hypothesis that the increased crack density rate related to variations in maximum cyclic load observed in [6]

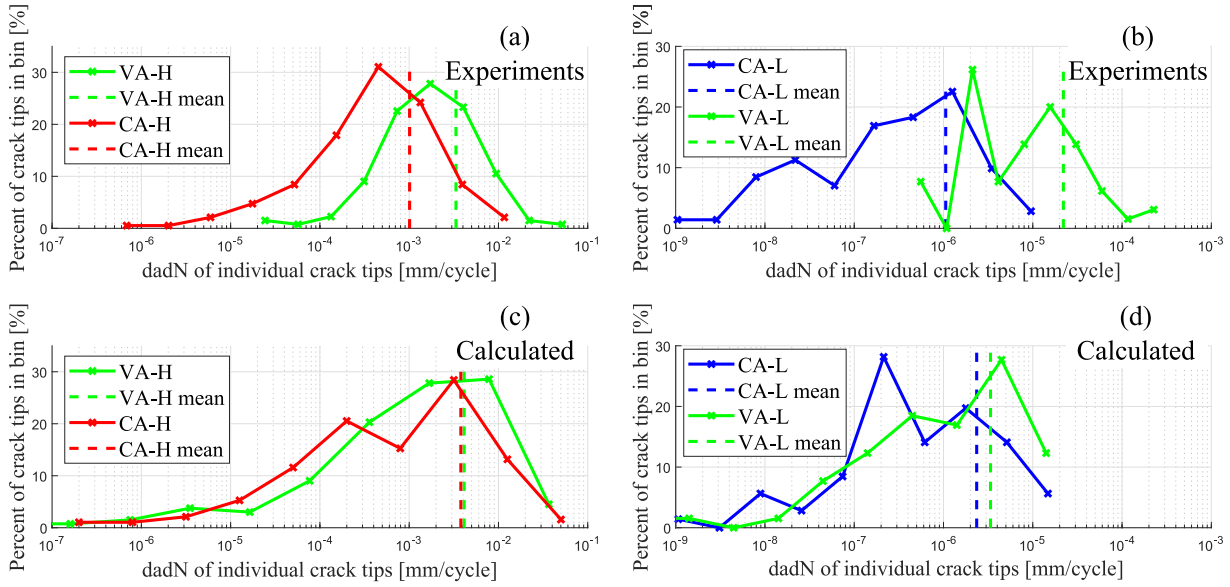

Fig. 13. Histogram of CGR based on images for (a) a high load block and (b) a constant rate phase, and histograms for CGR based Paris law-like relation and ERR, for (c) a high load block and (d) a constant rate phase. The dashed lines indicate the mean of the crack growth rate for each test. (For interpretation of the references to colour in this figure legend, the reader is referred to the web version of this article.)

can be explained by locally increased ERR, local decreases in fracture toughness due to diffuse damage, local variations in material toughness or a combination of the three. This is done by considering two research questions, which are answered below.

- It is shown that the ERR, in an average sense, is increased in VA load cases due to stress redistributions caused by the configuration of cracks, i.e., location, length, and the number of cracks. The CGR of the crack tips is also increased in the VA cases compared to the corresponding CA cases.
- The effect of the increased ERR on the CGR has been estimated by combining a Paris law-like expression linking the ERR and CGR from the CA tests and the numerically obtained ERR. This combination shows that less than 5% of the increased CGR can be explained through the increased ERR. Therefore, it stands to reason that the primary reason for the increased crack density rate and CGR is local decreases in fracture toughness due to diffuse damage and potentially material inhomogeneities causing the CGR to decrease in CA-L load cases.

CRediT authorship contribution statement

J.J. Bender: Software, Validation, Formal analysis, Investigation, Writing – original draft, Writing – review & editing. **B.L.V. Bak:** Conceptualization, Methodology, Writing – review & editing, Supervision. **L. Carreras:** Resources, Writing – review & editing. **E. Lindgaard:** Conceptualization, Methodology, Writing – review & editing, Supervision, Funding acquisition.

Declaration of competing interest

The authors declare that they have no known competing financial interests or personal relationships that could have appeared to influence the work reported in this paper.

Data availability

Data will be made available on request.

Acknowledgement

This work is supported by the Talent Management Programme at Aalborg University, Denmark (Internal grant number: 771120). This support is gratefully acknowledged.

References

[1] Degrieck J, Van Paepegem W. Fatigue damage modeling of fibre-reinforced composite materials: Review. Appl Mech Rev 2001;54(4):279–300. http://dx.doi.org/10.1115/1.1381395.

[2] Bak BLV, Sarrado C, Turon A, Costa J. Delamination under fatigue loads in composite laminates: A review on the observed phenomenology and computational methods. Appl Mech Rev 2014;66(6):060803. http://dx.doi.org/10.1115/1.4027647.

[3] Turon A, Bak BLV, Lindgaard E, Sarrado C, Lund E. 3 - Interface elements for fatigue-driven delaminations in advanced composite materials. In: Camanho PP, Hallett SRBT, editors. Woodhead publishing series in composites science and engineering. Numerical modelling of failure in advanced composite materials, Woodhead Publishing; 2015, p. 73–91.

[4] Ten Have AA. WISPER and WISPERX: Summary paper describing their backgrounds, derivation and statistics. In: American society of mechanical engineers, vol. 14, Solar Energy Division (Publication) SED; 1993, p. 169–78.

[5] ISO 13003 fibre-reinforced plastics – determination of fatigue properties under cyclic loading conditions. 2003.

[6] Bender JJ, Bak BLV, Jensen SM, Lindgaard E. Effect of variable amplitude block loading on intralaminar crack initiation and propagation in multidirectional GFRP laminate. Composites B 2021;217:108905. http://dx.doi.org/10.1016/j.compositesb.2021.108905.

[7] Jensen SM, Bak BLV, Bender JJ, Lindgaard E. Transition-behaviours in fatigue-driven delamination of GFRP laminates following step changes in block amplitude loading. Int J Fatigue 2021;144:106045. http://dx.doi.org/10.1016/j.ijfatigue.2020.106045.

[8] Jensen SM, Bak BLV, Bender JJ, Carreras L, Lindgaard E. Transient delamination growth in GFRP laminates with fibre bridging under variable amplitude loading in G-control. Composites B 2021;225(September):109296. http://dx.doi.org/10.1016/j.compositesb.2021.109296.

[9] Schaff JR, Davidson BD. Life prediction methodology for composite structures. Part I - Constant amplitude and two-stress level fatigue. J Compos Mater 1997;31(2):128–57. http://dx.doi.org/10.1177/002199839703100202.

[10] Schaff JR, Davidson BD. Life prediction methodology for composite structures. Part II - spectrum fatigue. J Compos Mater 1997;31(2):158–81.

[11] Filis PA, Farrow IR, Bond IP. Classical fatigue analysis and load cycle mix-event damage accumulation in fibre reinforced laminates. Int J Fatigue 2004;26(6):565–73. http://dx.doi.org/10.1016/j.ijfatigue.2003.10.013.

[12] Bourchak M, Farrow IR, Bond IP, Rowland CW, Menan F. Acoustic emission energy as a fatigue damage parameter for CFRP composites. Int J Fatigue 2007;29(3):457–70. http://dx.doi.org/10.1016/j.ijfatigue.2006.05.009.

[13] Post NL, Cain J, McDonald KJ, Case SW, Lesko JJ. Residual strength prediction of composite materials: Random spectrum loading. Eng Fract Mech 2008;75(9):2707–24. http://dx.doi.org/10.1016/j.engfracmech.2007.03.002.

[14] D'Amore A, Grassia L. A method to predict the fatigue life and the residual strength of composite materials subjected to variable amplitude (VA) loadings. Compos Struct 2019. http://dx.doi.org/10.1016/j.compstruct.2019.111338.

[15] Lubineau G, Ladevèze P. Towards a micromechanics-based damage mesomodel for CFRP laminates under thermomechanical cyclic loading. Sci Eng Compos Mater 2005;12(1–2):71–82. http://dx.doi.org/10.1515/secm.2005.12.1-2.71.

[16] Lubineau G, Ladevèze P, Violeau D. Durability of CFRP laminates under thermomechanical loading: A micro - meso damage model. Compos Sci Technol 2006;66(7–8):983–92. http://dx.doi.org/10.1016/j.compscitech.2005.07.031.

[17] Nouri H, Lubineau G, Traudes D. An experimental investigation of the effect of shear-induced diffuse damage on transverse cracking in carbon-fiber reinforced laminates. Compos Struct 2013;106:529–36. http://dx.doi.org/10.1016/j.compstruct.2013.06.026.

[18] Quaresimin M, Carraro PA, Maragoni L. Early stage damage in off-axis plies under fatigue loading. Compos Sci Technol 2016;128:147–54. http://dx.doi.org/10.1016/j.compscitech.2016.03.015.

[19] Din IU, Tu S, Hao P, Panier S, Khan KA, Umer R, et al. Sequential damage study induced in fiber reinforced composites by shear and tensile stress using a newly developed arcan fixture. J Mater Res Technol 2020;9(6):13352–64. http://dx.doi.org/10.1016/j.jmrt.2020.09.067.

[20] Aoki R, Higuchi R, Yokozeki T, Aoki K, Uchiyama S, Ogasawara T. Damage-mechanics mesoscale modeling of composite laminates considering diffuse and discrete ply damages: Effects of ply thickness. Compos Struct 2021;277(May):114609. http://dx.doi.org/10.1016/j.compstruct.2021.114609.

[21] Llobet J, Maimí P, Essa Y, Martin de la Escalera F. Progressive matrix cracking in carbon/epoxy cross-ply laminates under static and fatigue loading. Int J Fatigue 2019;119(July 2018):330–7. http://dx.doi.org/10.1016/j.ijfatigue.2018.10.008.

[22] Adam T, Gathercole N, Reiter H, Harris B. Life prediction for fatigue of T800/5245 carbon-fibre composites: II. Variable-amplitude loading. Int J Fatigue 1994;16(8):533–47. http://dx.doi.org/10.1016/0142-1123(94)90479-0.

[23] Van Paepegem W, Degrieck J. Effects of load sequence and block loading on the fatigue response of fiber-reinforced composites. Mech Adv Mater Struct 2002;9(1):19–35. http://dx.doi.org/10.1080/153764902317224851.

[24] Erpolat S, Ashcroft IAA, Crocombe ADD, Abdel-Wahab MMM. A study of adhesively bonded joints subjected to constant and variable amplitude fatigue. Int J Fatigue 2004;26(11):1189–96. http://dx.doi.org/10.1016/j.ijfatigue.2004.03.011.

[25] Sarfaraz R, Vassilopoulos AP, Keller T. Variable amplitude fatigue of adhesively-bonded pultruded GFRP joints. Int J Fatigue 2013;55:22–32. http://dx.doi.org/10.1016/j.ijfatigue.2013.04.024.

[26] Brod M, Dean A, Rolfes R. Numerical life prediction of unidirectional fiber composites under block loading conditions using a progressive fatigue damage model. Int J Fatigue 2021;147(October 2020):106159. http://dx.doi.org/10.1016/j.ijfatigue.2021.106159.

[27] Lam KY, Phua SP. Multiple crack interaction and its effect on stress intensity factor. Eng Fract Mech 1991;40(3):585–92. http://dx.doi.org/10.1016/0013-7944(91)90152-Q.

[28] Laures JP, Kachanov M. Three-dimensional interactions of a crack front with arrays of penny-shaped microcracks. Int J Fract 1991;48(4):255–79. http://dx.doi.org/10.1007/BF00012916.

[29] Wang YZ, Atkinson JD, Akid R, Parkins RN. Crack interaction, coalescence and mixed mode fracture mechanics. Fatigue Fract Eng Mater Struct 1996;19(4):427–39. http://dx.doi.org/10.1111/j.1460-2695.1996.tb00979.x.

[30] Glud JA, Dulieu-Barton JM, Thomsen OT, Overgaard LCT. Automated counting of off-axis tunnelling cracks using digital image processing. Compos Sci Technol 2016;125:80–9. http://dx.doi.org/10.1016/j.compscitech.2016.01.019.

[31] Maragoni L, Carraro PA, Peron M, Quaresimin M. Fatigue behaviour of glass/epoxy laminates in the presence of voids. Int J Fatigue 2017;95:18–28. http://dx.doi.org/10.1016/j.ijfatigue.2016.10.004.

[32] Shen H, Yao W, Qi W, Zong J. Experimental investigation on damage evolution in cross-ply laminates subjected to quasi-static and fatigue loading. Composites B 2017;120:10–26. http://dx.doi.org/10.1016/j.compositesb.2017.02.033.

[33] Bender JJ, Glud JA, Lindgaard E. Optical high dynamic range acquisition of crack density evolution in cyclic loaded GFRP cross-ply laminates affected by stitching. Composites A 2018;112:207–15. http://dx.doi.org/10.1016/j.compositesa.2018.05.032.

[34] Bak BLV, Lindgaard E. A method for automated digital image-based tracking of delamination fronts in translucent glass fibre-laminated composite materials. Strain 2020;56(4):1–12. http://dx.doi.org/10.1111/str.12345.

[35] Drvoderic M, Rettl M, Pletz M, Schuecker C. CrackDect: Detecting crack densities in images of fiber-reinforced polymers. SoftwareX 2021;16:100832. http://dx.doi.org/10.1016/j.softx.2021.100832.

[36] Raju IS, Sistla R, Krishnamurthy T. Fracture mechanics analyses for skin-stiffener debonding. Eng Fract Mech 1996;54(3):371–85. http://dx.doi.org/10.1016/0013-7944(95)00184-0.

[37] Trabal GG, Bak BLV, Chen B, Lindgaard E. An adaptive floating node based formulation for the analysis of multiple delaminations under quasi-static loading. Composites A 2022;156(August 2021):106846. http://dx.doi.org/10.1016/j.compositesa.2022.106846.

[38] Trabal GG, Bak BLV, Chen B, Carreras L, Lindgaard E. An adaptive floating node based formulation for the analysis of multiple delaminations under high cycle fatigue loading. Composites A 2022;160(June):107036. http://dx.doi.org/10.1016/j.compositesa.2022.107036.

[39] Trabal GG, Bak BLV, Chen B, Jensen SM, Lindgaard E. Delamination toughening of composite laminates using weakening or toughening interlaminar patches to initiate multiple delaminations: A numerical study. Eng Fract Mech 2022;108730. http://dx.doi.org/10.1016/j.engfracmech.2022.108730.

[40] Rice JR. A path independent integral and the approximate analysis of strain concentration by notches and cracks. J Appl Mech Trans ASME 1964;35(2):379–88. http://dx.doi.org/10.1115/1.3601206.

[41] Carreras L, Bak BLV, Turon A, Renart J, Lindgaard E. Point-wise evaluation of the growth driving direction for arbitrarily shaped delamination fronts using cohesive elements. Eur J Mech A Solids 2018;72(May):464–82. http://dx.doi.org/10.1016/j.euromechsol.2018.05.006.

[42] Carreras L, Lindgaard E, Renart J, Bak BLV, Turon A. An evaluation of mode-decomposed energy release rates for arbitrarily shaped delamination fronts using cohesive elements. Comput Methods Appl Mech Engrg 2019;347:218–37. http://dx.doi.org/10.1016/j.cma.2018.12.027.

[43] Carreras L, Turon A, Bak BLV, Lindgaard E, Renart J, Martin de la Escalera F, et al. A simulation method for fatigue-driven delamination in layered structures involving non-negligible fracture process zones and arbitrarily shaped crack fronts. Composites A 2019;122(April):107–19. http://dx.doi.org/10.1016/j.compositesa.2019.04.026, arXiv:1905.05000.

[44] Simonetto M, Carraro PA, Maragoni L, Quaresimin M. Crack initiation and evolution in glass/epoxy laminates under two-stage block loadings. Compos Sci Technol 2022;225(April):109504. http://dx.doi.org/10.1016/j.compscitech.2022.109504.

[45] Paris P, Erdogan F. A critical analysis of crack propagation laws. J Basic Eng 1963;85(4):528–33. http://dx.doi.org/10.1115/1.3656900.